RESEARCH ARTICLE
SPACE PHYSICS: IONOSPHERIC PHYSICS

Earth and Planetary Physics
8: 910–919, 2024
doi: 10.26464/epp2024073

Interhemispheric and longitudinal differences in the ionosphere–thermosphere coupling process during the May 2024 superstorm

WenBo Li[1,2], LiBo Liu[1,2,3*], YuYan Yang[4], TingWei Han[1,3], RongJin Du[1,3], RuiLong Zhang[1,2,3], HuiJun Le[1,2,3], and YiDing Chen[1,3,5]

[1]Key Laboratory of Earth and Planetary Physics, Institute of Geology and Geophysics, Chinese Academy of Sciences, Beijing 100029, China;

[2]Heilongjiang Mohe Observatory of Geophysics, Institute of Geology and Geophysics, Chinese Academy of Sciences, Beijing 100029, China;

[3]College of Earth and Planetary Sciences, University of Chinese Academy of Sciences, Beijing 100049, China;

[4]Institute of Space Weather, School of Atmospheric Physics, Nanjing University of Information Science and Technology, Nanjing 210044, China;

[5]Beijing National Observatory of Space Environment, Institute of Geology and Geophysics, Chinese Academy of Sciences, Beijing 100029, China

Key Points:

- A north–south hemispheric difference in the ionosphere and thermosphere was observed, notably in the Asian and American sectors, during the May 2024 superstorm.
- The north–south hemispheric difference in the total electron content (TEC) was strongly influenced by the thermospheric composition, density, and wind.
- The plasma transport from the topside or conjugate hemispheres is important in modulating north–south hemispheric differences in the TEC.

Citation: Li, W. B., Liu, L. B., Yang, Y. Y., Han, T. W., Du, R. J., Zhang, R. L., Le, H. J., and Chen, Y. D. (2024). Interhemispheric and longitudinal differences in the ionosphere–thermosphere coupling process during the May 2024 superstorm. *Earth Planet. Phys.*, *8*(6), 910–919. http://doi.org/10.26464/epp2024073

Abstract: Geomagnetic storm events have a strong influence on the ionosphere–thermosphere (I-T) coupling system. Analyzing the regional response process of the I-T system and its differences across the northern and southern hemispheres is an important but challenging task. In this study, we used a combination of multiple observations and a model simulation to examine the north–south hemispheric difference in the I-T coupling system in the American and Asian sectors during the geomagnetic superstorm that occurred in May 2024. Observations of the total electron content (TEC) showed that the Asian sector had negative storms in the northern hemisphere and positive storms in the southern hemisphere, a process that exacerbated the hemispheric differences in the TEC. However, both hemispheres of the American sector showed negative storms. The thermospheric composition changes also differed between the two sectors, and their variation could partially explain the hemispheric differences caused by positive and negative storms. Moreover, the influence of the thermospheric density change was less than that of the thermospheric composition. Finally, the dynamic effect of the thermospheric wind and the plasma transport processes strongly modulated the north–south differences in the TEC at nighttime in the American and Asian sectors, respectively, during this superstorm.

Keywords: geomagnetic superstorm; north–south hemispheric difference; total electron content; O/N_2; thermospheric wind; plasma transport

1. Introduction

After entering Solar Cycle 25, solar activity has gradually increased. A sequence of coronal mass ejections (CMEs) from active region AR3664 slammed Earth on May 10, 2024 (Day of Year [DOY] 131), triggering the strongest geomagnetic storm in more than 20 years. The considerable energy inflow during the geomagnetic storm could have led to extensive disturbances in the ionosphere–thermosphere (I-T) coupling system (e.g., Abdu, 1997; Kelley et al., 2003; Prölss, 2011; Koskinen et al., 2017). The preventive engineering efforts developed over the years prevented this disturbance from causing a disaster, to a certain extent. Nevertheless, this superstorm did affect navigation and power systems, forcing many industries to halt operations during it (O'Callaghan and Billings, 2024). Although extensive work has illustrated the responses of the I-T system and has involved physical processes during geomagnetic storms (e.g., Prölss, 1995, 2011;

First author: W. B. Li, llwwb@mail.iggcas.ac.cn
Correspondence to: L. B. Liu, liul@mail.iggcas.ac.cn
Received 29 JUL 2024; Accepted 24 SEP 2024.
First Published online 01 NOV 2024.

Abdu, 1997; Heelis, 2008; Liu LB and Wan WX, 2016; Zhang RL et al., 2017; Li WB et al., 2023b), accurately characterizing the response of the I-T system, particularly the regional features and hemispheric differences during various space weather events, remains a challenge (Zettergren et al., 2023).

Geomagnetic storms induce changes in the I-T system through chemical, dynamic, and electrodynamic mechanisms (e.g., Heelis, 2008; Prölss, 2011). The influences mentioned are greatly affected by the uneven distribution of the geomagnetic field and geographical space. This distribution leads to substantial variations across different longitude sectors and between the northern and southern hemispheres. Consequently, the I-T system exhibits diverse regional features (e.g., Liu H and Lühr, 2005; Bruinsma et al., 2006; Zhao BQ et al., 2007; Zhu QY et al., 2023). Within the geomagnetic coordinate system, electric fields map along magnetic field lines and extend to both the northern and southern hemispheres. This alignment results in simultaneous reactions in both hemispheres (Zhang SR et al., 2023). Disregarding the impact of the dynamic process, the effect of the electric field is typically symmetrical around the geomagnetic equator in the low latitudes, where electrodynamics has a strong influence. A notable example is the equatorial fountain effect during both storms and quiet times (Appleton, 1946; Mannucci et al., 2005). In contrast, a noticeable regional and hemispheric difference exists in neutral components and wind (e.g., Bruinsma et al., 2006; Zhang XF et al., 2017; Wu Q et al., 2019; Qian LY et al., 2023). This difference is mostly driven by variations in solar radiation and the amount of energy received at high latitudes (e.g., Ercha et al., 2012; Knipp et al., 2021; Pakhotin et al., 2021). Furthermore, the combination of storm-time circulation and background atmospheric circulation contributes to the unique regional response features observed across various longitudes (Prölss, 2011), thereby increasing the complexity of both regional and hemispheric variations. Hence, the variations in neutral components and dynamic processes strongly influence the regional and hemispheric features of the I-T system.

Examining the features of global-scale I-T systems is a crucial but difficult undertaking, necessitating the examination of both ionized and neutral components, with the latter being particularly challenging to acquire. Decades of effort in space science have enabled the ability to observe the I-T system simultaneously in parts of America and Asia. This breakthrough has made it feasible to conduct comprehensive investigations on a worldwide scale. In this study, we used a combination of ground-based and satellite observation devices, as well as empirical models derived from the accumulated observations, to investigate the reactions of the I-T system during the May 2024 superstorm. The objective of this work was to uncover the role of compositional disturbances and dynamic processes in the formation of sector disparities and hemisphere asymmetries.

2. Data and Methods

The Global Navigation Satellite Systems (GNSS) network, the Defense Meteorological Satellite Program (DMSP) F18 satellite, the Fabry–Pérot Interferometer (FPI), the Global-scale Observations of the Limb and Disk (GOLD; Correira et al., 2021) mission, the Global UltraViolet Imager onboard the Thermosphere Ionosphere Mesosphere Energetics and Dynamics satellite (TIMED/GUVI; Christensen et al., 2003), the Gravity Recovery And Climate Experiment Follow-On (GRACE-FO), Swarm-A/B, and the thermospheric mass density (TMD) deep learning (DL) empirical model are used to investigate the north–south hemispheric difference in the ionosphere and thermosphere during the superstorm that occurred on May 10, 2024.

The total electron content (TEC) observation primarily relied on the high-spatial-and high-temporal-resolution TEC product of the Massachusetts Institute of Technology Haystack Observatory (MIT-TEC; Vierinen et al., 2016) in the American sector. The complementary TEC observations of the Asian sector were obtained from the International GNSS Service (IGS) and the Beidou Ionospheric Observation Network (BION; Hu LH et al., 2017). The TEC derivation method is detailed in Liu LB et al. (2022), and we do not provide a description here. The DMSP F18 satellite acquired information on the state of the topside ionosphere during the superstorm.

The FPIs at Cachoeira Paulista (22.7°S, 45°W) and Millstone Hill (42.6°N, 71.5°W) provided thermospheric wind information from the Madrigal database (http://cedar.openmadrigal.org) for the American sector. The Mohe (53.5°N, 122.3°E; Li WB et al., 2021) and Xinglong (40.4°N, 117.6°E; Yuan W et al., 2010) FPIs provided thermospheric wind information for the Asian sectors.

Additionally, the GOLD and the TIMED/GUVI displayed the thermospheric composition information (column density ratio of atomic oxygen to molecular nitrogen [O/N_2]) variations during this superstorm in the American and Asian regions, respectively. Because of systematic deviations in the observations of the two instruments, our analysis focused solely on the relative change in O/N_2 for each sector. Furthermore, as a result of the orbital constraint of TIMED/GUVI, the observation of the southern hemisphere was restricted to approximately 23°S geographic latitude (GLAT) during the target period. Nevertheless, the data from GOLD indicated that the variance in O/N_2 within the hemisphere was restricted. Therefore, we retained the observations of TIMED/GUVI in the southern hemisphere as a reference. It is important to acknowledge that the observations of TIMED/GUVI provided only the highest recorded O/N_2 in the southern hemisphere at lower latitudes.

Finally, we give the TMD variations by using the observations of GRACE-FO, Swarm-A/B, and the DL model simulation in conjunction with real-time space environment conditions as a benchmark to evaluate the status of the thermosphere at 400 km. The DL model is an improved version based on Li WB et al. (2023a). By including additional interplanetary environment information (the solar wind and interplanetary magnetic field [IMF]), the model can better describe multiple response features of the TMD.

3. Results and Discussion

Figure 1 depicts the solar radiation conditions ($F_{10.7}$ and $F_{10.7a}$), interplanetary environment information (solar wind and IMF), and geomagnetic disturbance indices (longitudinally symmetric disturbance index derived for *H* components [SYM-*H*] and Auroral Electrojet index [*AE*]) during DOY 129–135 (May 8–14). The solar

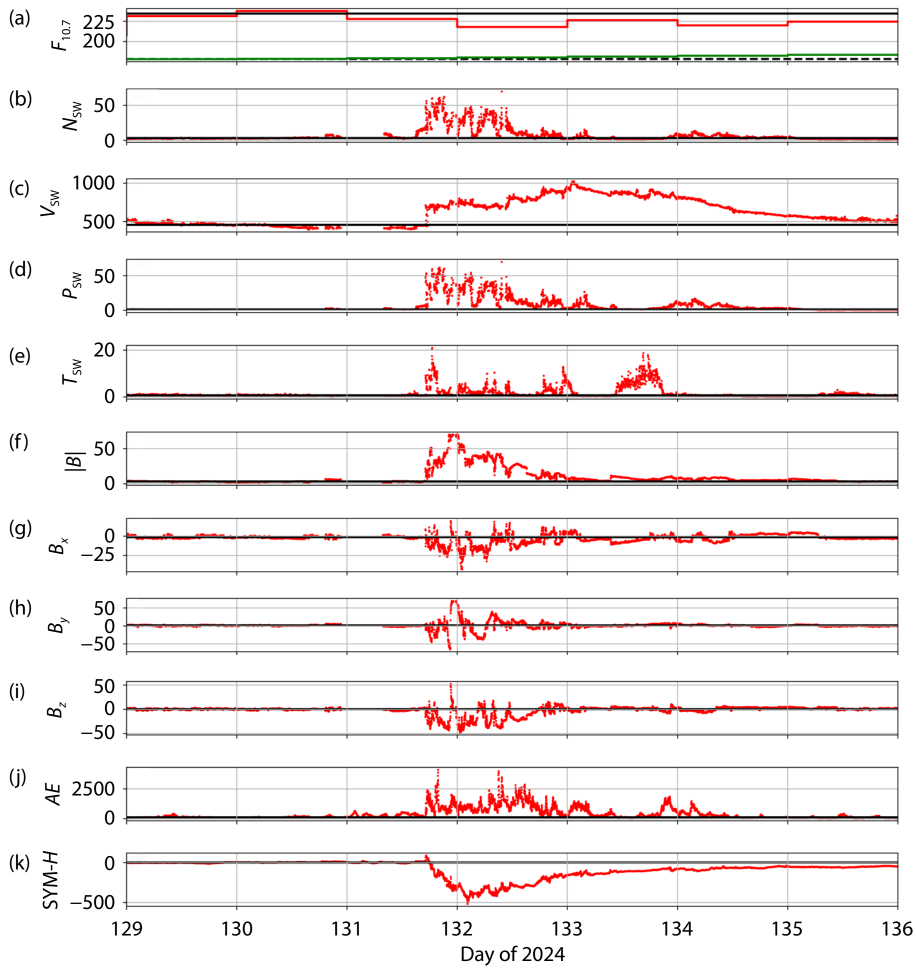

Figure 1. Variation in solar–terrestrial environmental conditions during DOY 129–135 (May 8–14), 2024. (a) $F_{10.7}$ (red, solar flux units [sfu]) and $F_{10.7a}$ (green, sfu); (b) solar wind proton density (N_{SW}, cm^{-3}); (c) solar wind speed (V_{SW}, km/s); (d) solar wind flow pressure (P_{SW}, nPa); (e) solar wind proton temperature (T_{SW}, 10^5 K); (f) IMF magnitude average (nT); (g) B_x (nT, GSM [Geocentric Solar Magnetospheric system]); (h) B_y (nT, GSM); (i) B_z (nT, GSM); (j) *AE* (nT); (k) SYM-*H* (nT). The red lines represent the observations, and the black lines indicate the quiet-time conditions for reference.

radiation conditions were stable during the superstorm event. The solar wind speed and IMF magnitude increased abruptly when the first CME arrived on DOY 131 (May 10). Following that event, the SYM-*H* index dropped rapidly to more than −500 nT on DOY 132 (May 11). The *AE* index indicated the presence of notable disturbances at high latitudes during DOY 131–132 (May 10–11). These disturbances strongly affected the condition of the thermosphere, resulting in further impacts on the ionosphere. To better evaluate the impact of the superstorm on the I-T system, we used the period of DOY 129–130 (May 8–9) as a baseline for quiet-time conditions.

3.1 The North–South Hemispheric Difference in TEC

For this work, we selected two specific longitude sectors and two latitude zones to investigate the responses of the I-T system in the northern and southern hemispheres. Figure 2 is a schematic depiction of the target regions. The Asian sector is located between 100 and 150°E geographic longitude (GLON), whereas the American sector is situated between 50 and 100°W GLON. The latitude zone selects geomagnetic latitudes (MLAT) ranging from 10 to 50°N for the northern hemisphere and from 10 to 50°S for the southern hemisphere. The TEC observations were abundant in these four regions and could provide relatively reliable information on ionosphere variations.

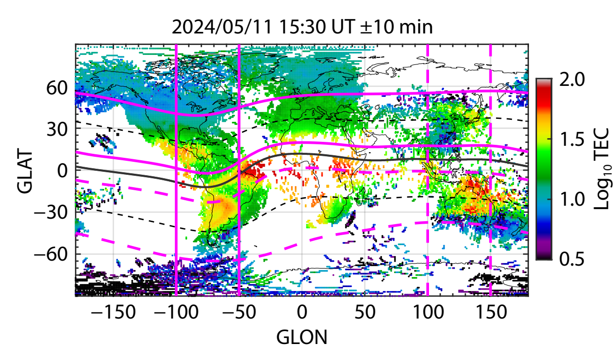

Figure 2. Schematic diagram of the selected target region, with solid and dashed pink lines framing the selected geomagnetic latitude regions for the northern and southern hemispheres and the selected geographic longitude regions for the Asian and American sectors. The background color diagram is the TEC observation distribution.

We set a one-hour window and computed the moving average for each hour in each region to examine the TEC variations. The northern and southern hemispheres were further divided into low and middle latitudes by 30°N and 30°S MLAT. Figure 3 shows the variations in regional average TEC in the American and Asian sectors during this superstorm. To calculate the north–south hemispheric difference ($TEC_{N\text{-}S}$), we subtracted the southern hemisphere TEC from the northern hemisphere TEC and divided the result by the total TEC of both hemispheres.

It can be seen that the ionospheric responses in the American and Asian sectors during this superstorm are considerably different. In the American sector, the diurnal variation in TEC shows similar features in both hemispheres, whereas the TEC in the northern hemisphere is systematically more than that in the southern hemisphere ($TEC_{N\text{-}S} > 0$). On DOY 132 (May 11), the $TEC_{N\text{-}S}$ decreased, especially in the middle latitudes. The $TEC_{N\text{-}S}$ saw a modest rise on DOY 133 (May 12), and then returned to the quiet-time level. In the Asian sector, a noticeable difference in the diurnal variations in TEC occurred between the northern and southern hemispheres. The TEC was greater in the southern hemisphere around midday and it decreased more rapidly in the afternoon, leading to lower TEC levels at nighttime. This difference in diurnal variation was consistent with the seasonal anomaly features of the TEC (Hunsucker and Hargreaves, 2002). According to the diurnal variation in the TEC, the $TEC_{N\text{-}S}$ of the Asian sector generally manifested as positive values, with negative values appearing only around noon. The $TEC_{N\text{-}S}$ of the Asian sector became negative during the superstorm. This pattern persisted consistently over the middle and low latitudes.

3.2 The Influence of Thermospheric Composition and Mass Density

Variations in the ionosphere during a superstorm are greatly influenced by the thermosphere, which serves as its background. Investigating the condition of the thermosphere aids in understanding the reasons for the formation of different responses in the ionosphere. Given the limited availability of thermospheric measurements, the thermospheric condition during this superstorm was investigated by using both observations and modeling. The TMD model results were compared with measurements taken by GRACE-FO (accelerometer result) and Swarm A/B (precise orbit determination result) during the superstorm. The TMD variations in the model were consistent with the observations, which indicates that the model results were reliable (Supplemental Figure S1). The TMD is greatly affected by altitude variations, and most satellites are at different altitudes in the northern and southern hemispheres. Therefore, we use the simulation results at a fixed altitude (400 km) for subsequent demonstration and discussion. Figure 4 illustrates variations in O/N_2 and TMD in the specific regions that correspond to the regional average TEC result.

Clear differences between the American and Asian sectors in the thermosphere conditions can be seen. During quiet time, the O/N_2 had a similar pattern between the northern and southern hemispheres of the two sectors, with O/N_2 values being slightly lower in the northern hemisphere than in the southern hemisphere. This feature is related to the thermospheric wind blowing from the summer (northern) hemisphere to the winter (southern)

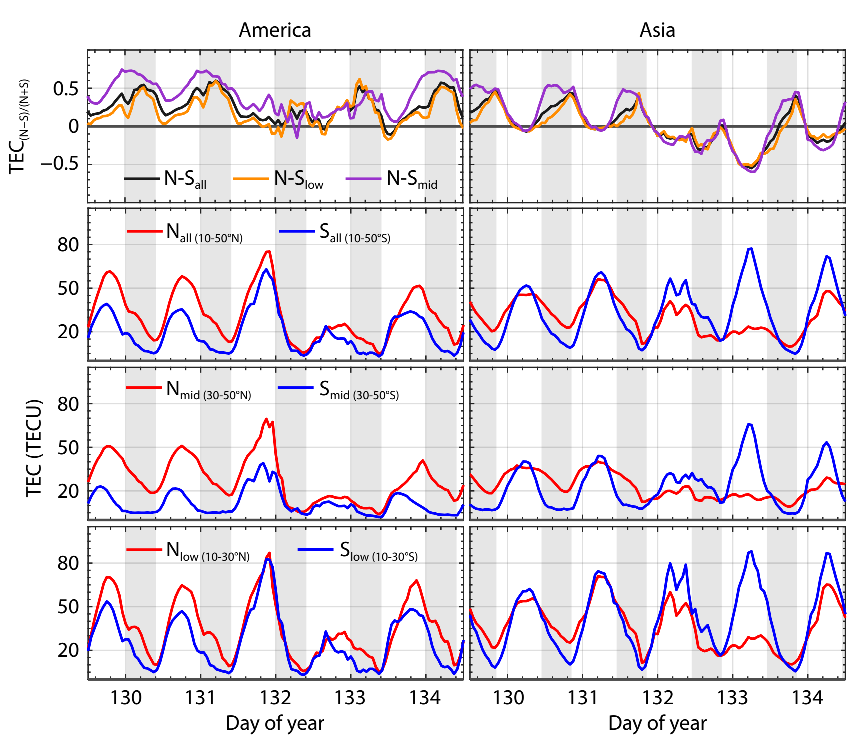

Figure 3. The northern and southern hemispheric TEC variations in the American and Asian sectors during the May 2024 geomagnetic superstorm. The left (right) column is the American (Asian) sector, and the red (blue) line is the regional average TEC for the northern (southern) hemisphere. The yellow, purple, and black lines in the top row show the differences between the northern and southern hemispheres at the low (10–30° MLAT), middle (30–50° MLAT), and overall latitudes (10–50° MLAT), respectively.

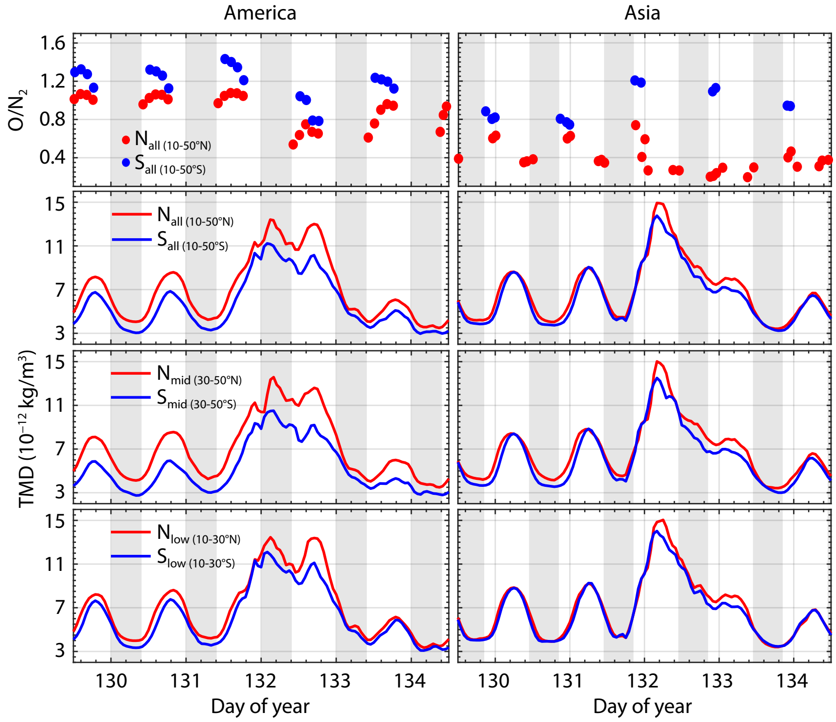

Figure 4. The northern and southern hemispheric thermospheric composition and mass density variations in the American and Asian sectors during the May 2024 geomagnetic superstorm. The left (right) column is the American (Asian) sector. The top panel shows the O/N_2 variations, with the American sector from GOLD observations and the Asian sector from TIMED/GUVI observations at 10–50° MLAT. The bottom three rows show the TMD variations at 400 km from the model at the low (10–30° MLAT), middle (30–50° MLAT), and overall latitudes (10–50° MLAT), respectively. The red (blue) lines are the regional average results for the northern (southern) hemisphere.

hemisphere (Qian LY et al., 2023; Wang ZH et al., 2023; Forbes et al., 2024). During the superstorm, the disturbance in O/N_2 appeared to be very different in the two longitude sectors. Since DOY 132 (May 11), the daytime O/N_2 in the southern hemisphere notably increased, whereas that in the northern hemisphere decreased around the Asian sector. This resulted in a notable increase in the north–south thermospheric composition difference. In the American sector, the O/N_2 of the northern and southern hemispheres decreased simultaneously, and no substantial change occurred in the O/N_2 differential between the two hemispheres compared with the quiet time.

During the daytime, the TEC variations correlated well with the O/N_2 changes. This change in O/N_2 is related to the ratio of production and loss of the ionizing component, and a lower O/N_2 means a stronger recombination loss. The variations in O/N_2 in the Asian sector were an important factor in controlling the occurrence of negative ionospheric storms in the northern hemisphere on DOY 132–133 (May 11–12). This process caused $TEC_{N\text{-}S}$ to reverse from positive to negative. Conversely, O/N_2 declined synchronously in both hemispheres of the American sector, which resulted in similar negative storms in both hemispheres. However, unlike the Asian sector, no drastic change occurred in $TEC_{N\text{-}S}$.

The variation in O/N_2 refers only to the change in the ratio of thermospheric components, whereas the change in TEC not only is related to the ratio of production and loss, but also is modulated by the background atmospheric density and temperature. Because of the lack of total overlap between MLAT and GLAT, the same MLAT range correlates to distinct GLAT ranges in the northern and southern hemispheres across various longitude sectors. Consequently, this results in differences in the background thermospheric conditions between the two hemispheres. The geomagnetic and geographical coordinates in the American sector exhibited more deviation compared with those in the Asian sector. This resulted in the 10–50° MLAT region the northern hemisphere being closer to the geographic equator and thus having greater atmospheric density. This difference also led to the fact that the TEC in the northern hemisphere of the American sector was consistently higher than the TEC in the southern hemisphere, and the difference was more pronounced in the middle latitudes of the American sector (Figure 4).

According to the TMD modeling results, no obvious difference occurred in the TMD change between the northern and southern hemispheres during the superstorm. The slight increase in TMD in the northern hemisphere may have been partly due to the increase in atmospheric density and may have been affected by the increase in the proportion of molecular components. Nevertheless, the contribution of variations in TMD to the north–south hemispheric difference in the TEC was not as strong as the effect of changes in thermospheric components during this superstorm.

3.3 The Contribution of Dynamic Processes

Through an examination of the thermospheric composition and density, we were able to elucidate some aspects of the difference between the northern and southern hemispheres in the I-T system during the superstorm. However, these evaluations mostly concentrated on the daytime. During the nighttime, when photochemical processes were not under control, the influence of dynamics on the north–south hemispheric difference became more apparent and stronger. Because of the scarcity of thermospheric wind measurements, we relied on a limited number of FPI observations during the nighttime to qualitatively examine the dynamic processes in each region.

In the American sector, we noted that the north–south hemispheric differences in TEC in the middle latitudes of DOY 132 (May 11) decreased substantially at nighttime and that this feature disappeared on DOY 133 (May 12). Figure 5 shows the TEC variations at nighttime in the American sector. The thermospheric wind detected by the Cachoeira Paulista (22.7°S, 45°W) and Millstone Hill (42.6°N, 71.5°W) FPIs is shown by magenta arrows. On DOY 132 (May 11), a strong disturbed wind could be seen, particularly a powerful westward wind that could be found in both hemispheres. On DOY 133 (May 12), the northern hemisphere disturbed wind slightly weakened and maintained its direction. In contrast, the thermospheric wind in the southern hemisphere shifted from westward to eastward. The increased symmetry of the thermospheric wind on DOY 132 (May 11) led to a greater similarity in dynamic effects, which in turn reduced the north–south hemispheric difference in TEC.

Thermospheric wind observations in the Asian sector were obtained from only two locations in the northern hemisphere: Mohe (53.5°N, 122.3°E) and Xinglong (40.4°N, 117.6°E). Hence, it was challenging to directly examine the effect of thermospheric wind between the northern and southern hemispheres. However, we have seen that more factors may be at play besides the effects of thermospheric winds. Figure 6 exhibits the variations in TEC and thermospheric wind in the Asian sector during the nighttime of DOY 132 (May 11). During this period, we discovered a noteworthy feature: the southern and northern hemispheres exhibited a region with enhanced TEC that was symmetrical according to the geomagnetic equator. The TEC enhancement region moved from eastern Asia to western Asia and lasted overnight. Before sunrise, the southern hemisphere had a higher TEC than the northern hemisphere. Simultaneously, the predominant thermospheric wind in the northern hemisphere was mostly westward. The TEC enhancement of the northern hemisphere at nighttime gradually reduced the north–south hemispheric difference in TEC.

Several theoretical explanations have been proposed for the ionospheric nighttime enhancement, such as an uplift of the ionosphere by the thermospheric wind, plasma transport across hemispheres, and injection from the top ionosphere or plasmasphere (He MS et al., 2009; Chen YD et al., 2015; Li WB et al., 2020). Among them, the effect of the thermospheric wind is to lift the ionosphere to a higher altitude with a lower recombination loss rate, thus slowing down the recombination loss of electron density. For periods with a complete loss of photoionization, it is difficult to increase the TEC by the effect of only the thermospheric wind. Hence, it is necessary to take into account other plasma transport mechanisms.

Considering that the TEC enhancement regions of the two hemispheres in Figure 6 have good symmetry according to the geomagnetic equator, the source of the enhancement in the northern hemisphere is likely the transport through the magnetic field lines. The source region could come from either the topside or the conjugate hemispheres. In the daytime, the plasma is carried to the protonosphere from the ionosphere, whereas during the nighttime, the protonosphere is used as the source

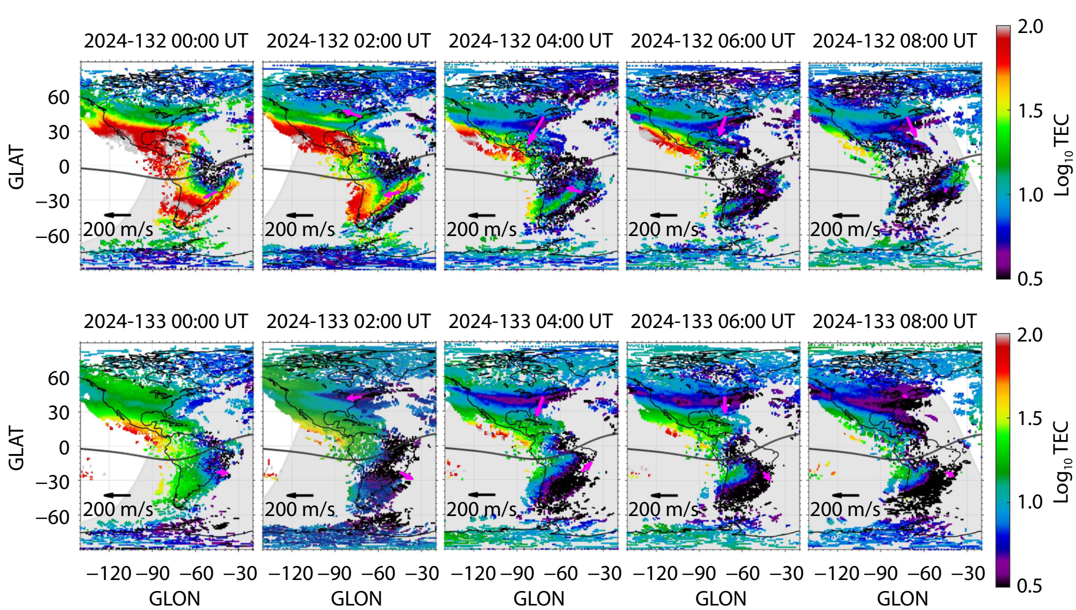

Figure 5. The TEC and thermospheric wind variation in the American sector during the nighttime of DOY 132 and 133 (May 11 and 12). The background color diagram is the TEC observation distribution. The magenta arrows are the thermospheric wind observed by the FPIs. The black arrows give the scale of the thermospheric wind.

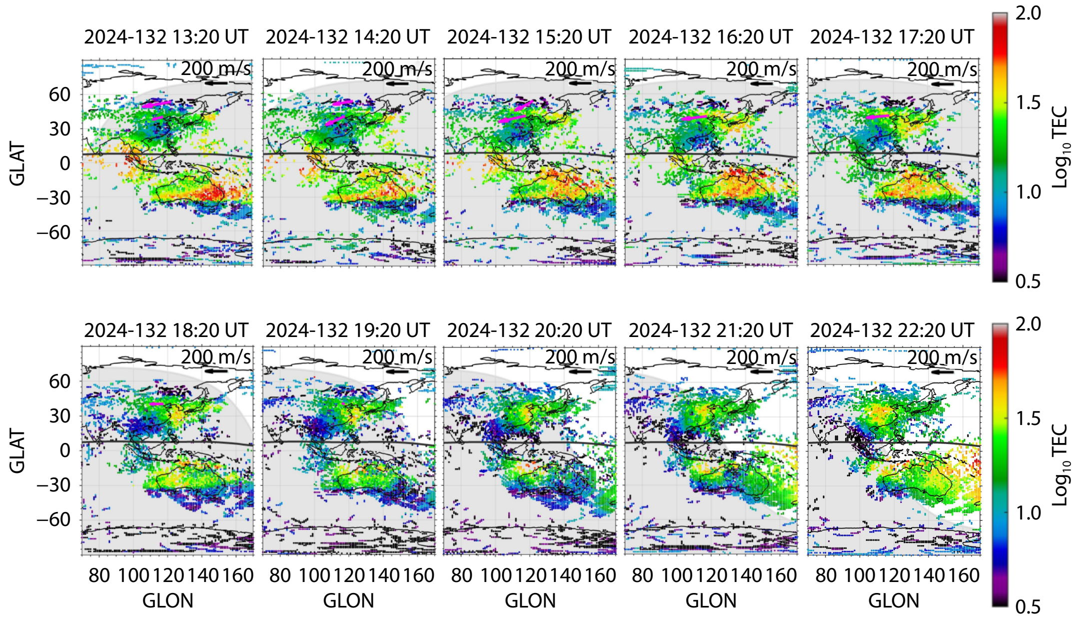

Figure 6. The TEC and thermospheric wind variation in the Asian sector during the nighttime of DOY 132 (May 11). The background color diagram is the TEC observation distribution. The magenta arrows are the thermospheric wind observed by the FPIs. The black arrows give the scale of the thermospheric wind.

region to maintain the ionosphere. Meanwhile, the winter hemisphere benefits from the conjugate region in the summer hemisphere during quiet-time conditions (Hunsucker and Hargreave, 2002). Figure 4 demonstrates a higher TMD, which generally corresponds to a higher thermosphere temperature. The higher temperatures expand the atmosphere and make it easier for the protonosphere to store more plasma during the daytime. Supplemental Figure S2 shows the observations of DMSP F18 (~857 km). The ratio of O^+ density to total ion density (O^+/N_i) at the topside ionosphere in the Asian sector increased substantially during the nighttime of DOY 132 (May 11), which also demonstrated that more plasma from a low altitude was transported to higher altitudes. This means that more raw materials could be made available for ionospheric nighttime enhancement. In addition, there was a downward drift velocity in the southern hemisphere and a slightly weakened upward transport in the northern hemisphere. This result supports plasma injection processes from higher altitudes. However, note that the observed period of DMSP F18 is later than the main phase of the ionospheric nighttime enhancement in the northern hemisphere, which may be the reason no substantial downward drift velocity was observed in the northern hemisphere. Furthermore, the analysis of the relative variation in TEC [$dTEC = (TEC - TEC_{quiet\text{-}time})/TEC_{quiet\text{-}time}$] revealed a drop in dTEC in the southern hemisphere as dTEC in the northern hemisphere increased (Supplemental Figure S3). This finding seems to support a transport process from the southern hemisphere to the northern hemisphere. Determining which of the previously indicated transport processes is more prominent requires more observation or further validation through theoretical model simulations. Nevertheless, it is indisputable that the north–south hemispheric difference in TEC is additionally influenced by these external plasma transport processes.

4. Conclusions

For this study, we utilized a combination of observation and model simulation to investigate the north–south hemispheric differences in the I-T coupling system in the American and Asian sectors during the geomagnetic superstorm in May 2024. The primary findings may be summarized as follows:

(1) In the Asian sector, the northern hemisphere exhibited an ionospheric negative storm at middle to low latitudes on DOY 132–133 (May 11–12), whereas the southern hemisphere had a positive storm at low latitudes on DOY 132 (May 11) and at middle to low latitudes on DOY 133 (May 12). In contrast, the American sector experienced ionospheric negative storms at middle to low latitudes in both hemispheres on DOY 132–133 (May 11–12). This different response resulted in greater variation in the north–south hemispheric difference in TEC in the Asian sector than in the American sector during the superstorm.

(2) The variations in thermospheric composition during the superstorm were different in the Asian and American sectors. The O/N_2 showed a decrease in the northern hemisphere and an increase in the southern hemisphere within the Asian region. The O/N_2 ratio in both hemispheres of the American sector decreased synchronously. The thermospheric composition changes partially accounted for the variations in the north–south hemispheric difference in the TEC in the American and Asian sectors. The influence of variations in thermospheric composition had a greater effect on the north–south hemispheric difference in the TEC than did changes in the background thermospheric density.

(3) During this superstorm, the dynamic effect of the thermospheric wind modulated the variations in the north–south hemispheric difference in TEC in the American sector on DOY 132–133 (May 11–12). In the Asian region, the plasma transport process from the

topside or conjugate hemisphere played a substantial role in the variation in TEC between the northern and southern hemispheres on DOY 132 (May 11).

Acknowledgments

This research was supported by the National Natural Science Foundation of China (Grant Nos. 42030202, 42241115, and 42174204), the China Postdoctoral Science Foundation (Grant No. 2023M743467), the Youth Innovation Promotion Association of the Chinese Academy of Sciences (Grant No. Y202021), the National Key R&D Program of China (Grant No. 2022YFF0504400), and the Opening Funding of the Chinese Academy of Sciences dedicated to the Chinese Meridian Project. We acknowledge the use of data from the Chinese Meridian Project and the Solar–Terrestrial Environment Research Network (STERN) of the Chinese Academy of Sciences, which supported the Mohe FPI operation.

The interplanetary environmental information, $F_{10.7}$, and geomagnetic activity index can be accessed from the OMNI website (https://cdaweb.gsfc.nasa.gov/pub/data/omni/) and the World Data Center for Geomagnetism, Kyoto website (https://wdc.kugi.kyoto-u.ac.jp/wdc/Sec3.html). The MIT-TEC observation and the Cachoeira Paulista and Millstone Hill FPIs were provided from the Massachusetts Institute of Technology Haystack Observatory Madrigal database (http://cedar.openmadrigal.org/ftp/). The other TEC data were provided from the IGS FTP site (ftp://gdc.cddis.eosdis.nasa.gov/). The TIMED/GUVI data are available from their website (http://guvitimed.jhuapl.edu/data_fetch_l3_on2_idlsave). The GOLD data are available from the GOLD website (https://gold.cs.ucf.edu/data/search/). The Mohe FPI observations can be accessed at the World Data Center for Geophysics, Beijing (http://www.geophys.ac.cn/). The Xinglong FPI observations were provided by the Chinese Meridian Project (https://data.meridian-project.ac.cn/). The DMSP data are available on the National Centers for Environmental Information website (https://www.ncei.noaa.gov/data/dmsp-space-weather-sensors/access/), and the GRACE-FO and Swarm-A/B data are available on the TUDelft thermosphere data website (http://thermosphere.tudelft.nl).

Supplemental Materials

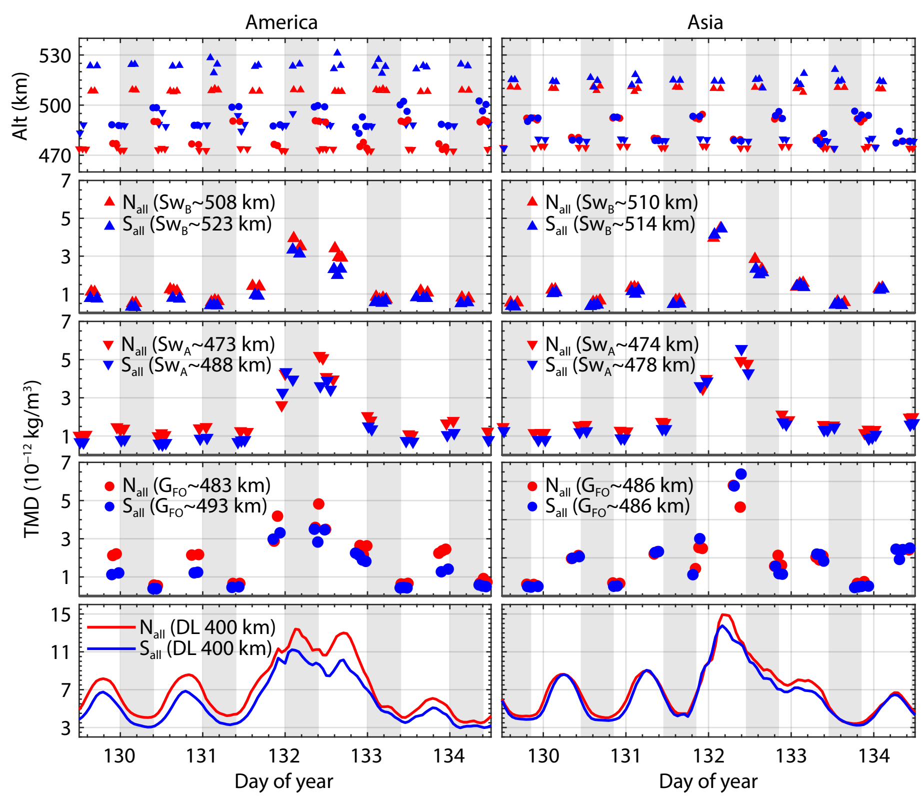

Figure S1. The observation and simulation regional average thermosphere mass density (TMD) variation in the American and Asian sectors. The top panel shows the altitude (Alt) of Swarm-A/B and GRACE-FO over each target region. The three panels in the middle show the TMD observations of the three: Swarm-B (Sw_B), Swarm-A (Sw_A), and GRACE-FO (G_{FO}), respectively. The TMD of Swarm-A/B observations are precise orbit determination results, and the TMD of GRACE-A is accelerometer results. The bottom panel shows the deep learning (DL) model simulation results at 400 km. The red (blue) lines and marks represent the TMD for the northern (southern) hemisphere.

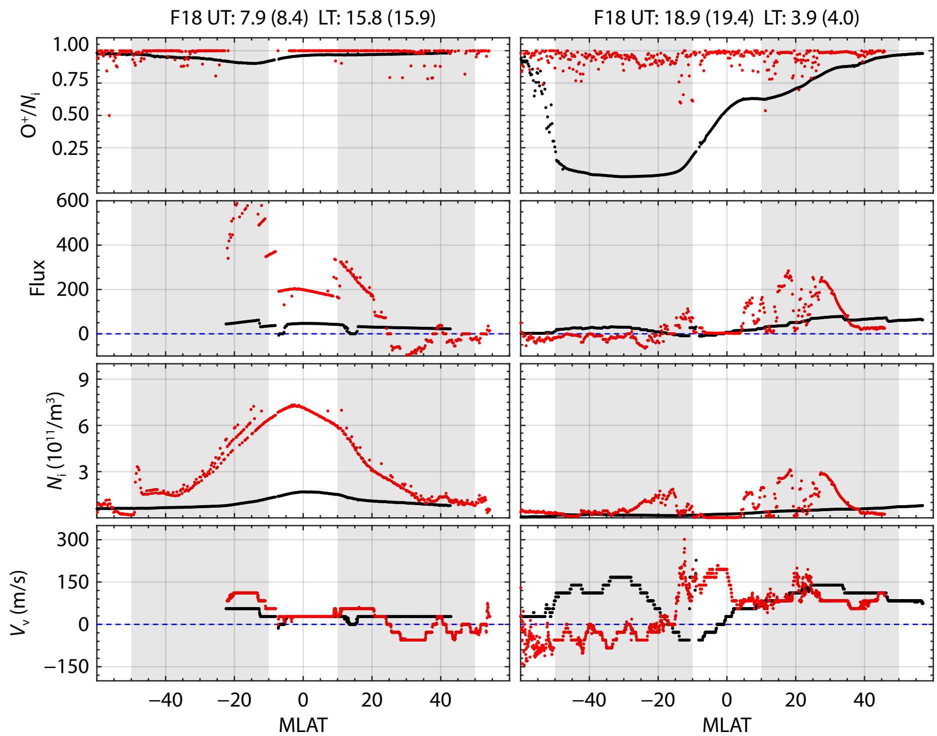

Figure S2. The regional average ratio of O^+ density to total ion density (O^+/N_i), plasma flux (Flux = $V_v \times N_i$), total ion density (N_i) and vertical ion drift velocity (V_v) variation observed by DMSP F18 (~857 km) at the Asian sectors. The red and black lines represent observations during DOY 132 (May 11) and DOY 130 (May 9), respectively. The left column shows the daytime orbital result, and the right column shows the nighttime orbital result. The top labels indicate the mean universal time (UT) and local time (LT) of the orbital result during DOY 132 (DOY 130).

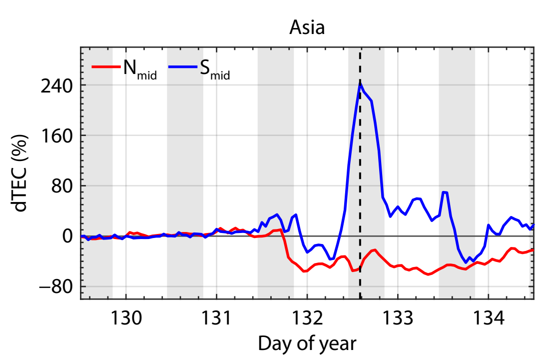

Figure S3. The relative variation in TEC [dTEC = (TEC − $TEC_{quiet\text{-}time}$)/$TEC_{quiet\text{-}time}$] variation at the Asia middle-latitude region. The red (blue) line represents the dTEC for the northern (southern) hemisphere.

References

Abdu, M. A. (1997). Major phenomena of the equatorial ionosphere-thermosphere system under disturbed conditions. *J. Atmos. Sol.-Terr. Phys.*, *59*(13), 1505–1519. https://doi.org/10.1016/s1364-6826(96)00152-6

Appleton, E. V. (1946). Two anomalies in the ionosphere. *Nature*, *157*(3995), 691–691. https://doi.org/10.1038/157691a0

Bruinsma, S., Forbes, J. M., Nerem, R. S., and Zhang, X. L. (2006). Thermosphere density response to the 20–21 November 2003 solar and geomagnetic storm from CHAMP and GRACE accelerometer data. *J. Geophys. Res.: Space Phys.*, *111*(A6), A06303. https://doi.org/10.1029/2005JA011284

Chen, Y. D., Liu, L. B., Le, H. J., Wan, W. X., and Zhang, H. (2015). N_mF_2 enhancement during ionospheric F_2 region nighttime: A statistical analysis based on COSMIC observations during the 2007–2009 solar minimum. *J. Geophys. Res.: Space Phys.*, *120*(11), 10083–10095. https://doi.org/10.1002/2015JA021652

Christensen, A. B., Paxton, L. J., Avery, S., Craven, J., Crowley, G., Humm, D. C., Kil, H., Meier, R. R., Meng, C. I., … Zhang, Y. M. (2003). Initial observations with the Global Ultraviolet Imager (GUVI) in the NASA TIMED satellite mission. *J. Geophys. Res.: Space Phys.*, *108*(A12), 1451. https://doi.org/10.1029/2003JA009918

Correira, J., Evans, J. S., Lumpe, J. D., Krywonos, A., Daniell, R., Veibell, V., McClintock, W. E., and Eastes, R. W. (2021). Thermospheric composition and solar EUV flux from the global-scale observations of the limb and disk (GOLD) mission. *J. Geophys. Res.: Space Phys.*, *126*(12), e2021JA029517. https://doi.org/10.1029/2021JA029517

Ercha, A., Ridley, A. J., Zhang, D. H., and Xiao, Z. (2012). Analyzing the hemispheric asymmetry in the thermospheric density response to geomagnetic storms. *J. Geophys. Res.: Space Phys.*, *117*(A8), A08317. https://doi.org/10.1029/2011JA017259

Forbes, J. M., Zhang, X. L., Maute, A., and Cullens, C. (2024). Responses of the mean thermosphere circulation, O/N_2 ratio and Ne to solar and magnetospheric forcing from above and tidal forcing from below. *J. Geophys. Res.: Space Phys.*, *129*(3), e2024JA032449. https://doi.org/10.1029/2024JA032449

He, M. S., Liu, L. B., Wan, W. X., Ning, B. Q., Zhao, B. Q., Wen, J., Yue, X., and Le, H. J. (2009). A study of the Weddell Sea Anomaly observed by FORMOSAT-3/COSMIC. *J. Geophys. Res.: Space Phys.*, *114*(A12), A12309. https://doi.org/10.1029/2009JA014175

Heelis, R. A. (2008). Low- and middle-latitude ionospheric dynamics associated with magnetic storms. In P. M. Kintner Jr., et al. (Eds.), *Midlatitude Ionospheric Dynamics and Disturbances* (pp. 51–61). Washington, DC: American Geophysical Union. https://doi.org/10.1029/181GM06

Hu, L. H., Yue, X. N., and Ning, B. Q. (2017). Development of the Beidou ionospheric observation network in China for space weather monitoring. *Space Weather*, *15*(8), 974–984. https://doi.org/10.1002/2017SW001636

Hunsucker, R. D., and Hargreaves, J. K. (2002). *The High-Latitude Ionosphere and Its Effects on Radio Propagation*. Cambridge, UK: Cambridge University Press.

https://doi.org/10.1017/CBO9780511535758

Kelley, M. C., Makela, J. J., Chau, J. L., and Nicolls, M. J. (2003). Penetration of the solar wind electric field into the magnetosphere/ionosphere system. *Geophys. Res. Lett.*, *30*(4), 1158. https://doi.org/10.1029/2002GL016321

Knipp, D., Kilcommons, L., Hairston, M., and Coley, W. R. (2021). Hemispheric asymmetries in Poynting flux derived from DMSP spacecraft. *Geophys. Res. Lett.*, *48*(17), e2021GL094781. https://doi.org/10.1029/2021GL094781

Koskinen, H. E. J., Baker, D. N., Balogh, A., Gombosi, T., Veronig, A., and von Steiger, R. (2017). Achievements and challenges in the science of space weather. *Space Sci. Rev.*, *212*(3), 1137–1157. https://doi.org/10.1007/s11214-017-0390-4

Li, W. B., Chen, Y. D., Liu, L. B., Le, H. J., Zhang, R. L., Li, J. C., and Huang, C. (2020). A statistical study on the winter ionospheric nighttime enhancement at middle latitudes in the Northern Hemisphere. *J. Geophys. Res.: Space Phys.*, *125*(7), e2020JA027950. https://doi.org/10.1029/2020JA027950

Li, W. B., Chen, Y. D., Liu, L. B., Trondsen, T. S., Unick, C., Wyatt, D., Ning, B. Q., Li, G. Z., Huang, C., … Le, H. J. (2021). Variations of thermospheric winds observed by a Fabry–Perot interferometer at Mohe, China. *J. Geophys. Res.: Space Phys.*, *126*(2), e2020JA028655. https://doi.org/10.1029/2020JA028655

Li, W. B., Liu, L. B., Chen, Y. D., Xiao, Z. W., Le, H. J., and Zhang, R. L. (2023a). Improving the extraction ability of thermospheric mass density variations from observational data by deep learning. *Space Weather*, *21*(7), e2022SW003376. https://doi.org/10.1029/2022SW003376

Li, W. B., Liu, L. B., Chen, Y. D., Yang, Y. Y., Han, T. W., Ding, F., Le, H. J., and Zhang, R. L. (2023b). Multi-instruments observation of ionospheric–thermospheric dynamic coupling over Mohe (53.5°N, 122.3°E) during the April 2023 geomagnetic storm. *J. Geophys. Res.: Space Phys.*, *128*(12), e2023JA032141. https://doi.org/10.1029/2023JA032141

Liu, H., and Lühr, H. (2005). Strong disturbance of the upper thermospheric density due to magnetic storms: CHAMP observations. *J. Geophys. Res.: Space Phys.*, *110*(A9), A09S29. https://doi.org/10.1029/2004JA010908

Liu, L. B., and Wan, W. X. (2016). New understanding achieved from 2 years of Chinese ionospheric investigations. *Sci. Bull.*, *61*(7), 524–542. https://doi.org/10.1007/s11434-016-1035-9

Liu, L. B., Yang, Y. Y., Le, H. J., Chen, Y. D., Zhang, R. L., Zhang, H., Sun, W. J., and Li, G. Z. (2022). Unexpected regional zonal structures in low latitude ionosphere call for a high longitudinal resolution of the global ionospheric maps. *Remote Sens.*, *14*(10), 2315. https://doi.org/10.3390/rs14102315

Mannucci, A. J., Tsurutani, B. T., Iijima, B. A., Komjathy, A., Saito, A., Gonzalez, W. D., Guarnieri, F. L., Kozyra, J. U., and Skoug, R. (2005). Dayside global ionospheric response to the major interplanetary events of October 29–30, 2003 "Halloween Storms". *Geophys. Res. Lett.*, *32*(12), L12S02. https://doi.org/10.1029/2004GL021467

O'Callaghan, J., and Billings, L. (2024). The strongest solar storm in 20 years did little damage, but worse space weather is coming. Scientific American. Retrieved May 16, 2024, from https://www.scientificamerican.com/article/the-strongest-solar-storm-in-20-years-did-little-damage-but-worse-space/

Pakhotin, I. P., Mann, I. R., Xie, K., Burchill, J. K., and Knudsen, D. J. (2021). Northern preference for terrestrial electromagnetic energy input from space weather. *Nat. Commun.*, *12*(1), 199. https://doi.org/10.1038/s41467-020-20450-3

Prölss, G. W. (1995). Ionospheric F-region storms. In H. Volland (Ed.), *Handbook of Atmospheric Electrodynamics* (*1995*) (pp. 195–248). Boca Raton, Florida: CRC Press.

Prölss, G. W. (2011). Density perturbations in the upper atmosphere caused by the dissipation of solar wind energy. *Surv. Geophys.*, *32*(2), 101–195. https://doi.org/10.1007/s10712-010-9104-0

Qian, L. Y., Yu, W. D., Pedatella, N., Yue, J., and Wang, W. B. (2023). Hemispheric asymmetry of the annual and semiannual variation of thermospheric composition. *J. Geophys. Res.: Space Phys.*, *128*(5), e2022JA031077. https://doi.org/10.1029/2022JA031077

Vierinen, J., Coster, A. J., Rideout, W. C., Erickson, P. J., and Norberg, J. (2016). Statistical framework for estimating GNSS bias. *Atmos. Meas. Tech.*, *9*(3), 1303–1312. https://doi.org/10.5194/amt-9-1303-2016

Wang, Z. H., Zou, S. S., and Cai, X. G. (2023). Hemispheric asymmetries in thermospheric composition and temperature: GOLD observations. *J. Geophys. Res.: Space Phys.*, *128*(10), e2023JA031868. https://doi.org/10.1029/2023JA031868

Wu, Q., Sheng, C., Wang, W. B., Noto, J., Kerr, R., McCarthy, M., Huang, C., Zhang, X. X., and Sarris, T. (2019). The midlatitude thermospheric dynamics from an interhemispheric perspective. *J. Geophys. Res.: Space Phys.*, *124*(10), 7971–7983. https://doi.org/10.1029/2019JA026967

Yuan, W., Xu, J. Y., Ma, R. P., Wu, Q., Jiang, G. Y., Gao, H., Liu, X., and Chen, S. Z. (2010). First observation of mesospheric and thermospheric winds by a Fabry–Perot interferometer in China. *Chin. Sci. Bull.*, *55*(35), 4046–4051. https://doi.org/10.1007/s11434-010-4192-2

Zettergren, M., Ozturk, D., Liu, H. L., Huba, J., Deng, Y., Snively, J., Fang, T. W., Ridley, A., Maute, A., … Hirsch, M. (2023). Physics-based ionosphere–thermosphere–mesosphere modeling: Status and future needs. *Bull. Am. Astron. Soc.*, *55*(3), 445. https://doi.org/10.3847/25c2cfeb.03c22216

Zhang, R. L., Liu, L. B., Le, H. J., Chen, Y. D., and Kuai, J. W. (2017). The storm time evolution of the ionospheric disturbance plasma drifts. *J. Geophys. Res.: Space Phys.*, *122*(11), 11665–11676. https://doi.org/10.1002/2017JA024637

Zhang, S. R., Nishimura, Y., Vierinen, J., Lyons, L. R., Knipp, D. J., Gustavsson, B. J., Waghule, B. V., Erickson, P. J., Coster, A. J., … Spicher, A. (2023). Simultaneous global ionospheric disturbances associated with penetration electric fields during intense and minor solar and geomagnetic disturbances. *Geophys. Res. Lett.*, *50*(19), e2023GL104250. https://doi.org/10.1029/2023GL104250

Zhang, X. F., Liu, L. B., and Liu, S. T. (2017). Dependence of thermospheric zonal winds on solar flux, geomagnetic activity, and hemisphere as measured by CHAMP. *J. Geophys. Res.: Space Phys.*, *122*(8), 8893–8914. https://doi.org/10.1002/2016JA023715

Zhao, B. Q., Wan, W. X., Liu, L. B., and Mao, T. (2007). Morphology in the total electron content under geomagnetic disturbed conditions: Results from global ionosphere maps. *Ann. Geophys.*, *25*(7), 1555–1568. https://doi.org/10.5194/angeo-25-1555-2007

Zhu, Q. Y., Lu, G., Lei, J. H., Deng, Y., Doornbos, E., van den IJssel, J., and Siemes, C. (2023). Interhemispheric asymmetry of the thermospheric neutral density response to the 7–9 September 2017 geomagnetic storms. *Geophys. Res. Lett.*, *50*(11), e2023GL103208. https://doi.org/10.1029/2023GL103208